Measurement 245 (2025) 116576

Contents lists available at ScienceDirect

Measurement

journal homepage: www.elsevier.com/locate/measurement

A novel robotic cell for the hot forging wire arc additive manufacturing process: Vibration analysis and process parameter investigation

Nuno Mendes [a,b,*], Henrique Barros [a], Miguel A. Machado [a,b], João P. Oliveira [a,c], Valdemar R. Duarte [a,b], Telmo G. Santos [a,b]

[a] UNIDEMI, Department of Mechanical and Industrial Engineering, NOVA School of Science and Technology, Universidade NOVA de Lisboa, 2829-516 Caparica, Portugal
[b] Laboratório Associado de Sistemas Inteligentes, LASI, 4800-058 Guimarães, Portugal
[c] CENIMAT/I3N, Department of Materials Science, NOVA School of Science and Technology, Universidade NOVA de Lisboa, 2829-516 Caparica, Portugal

ARTICLE INFO

Keywords:
Hot forging wire arc additive manufacturing
WAAM parameters
Robot vibration
Industrial robotics
Robotic cell design
Manufacturing process definition

ABSTRACT

This study presents the development and testing of a novel robotic cell designed for Hot Forging Wire Arc Additive Manufacturing (HF-WAAM). The HF-WAAM process integrates hot forging during the material deposition phase, offering improved dimensional accuracy and mechanical properties compared to conventional WAAM processes. A key focus of the research is the impact of robot vibration on the quality of the manufactured parts. Experiments were conducted to analyze process parameters for both WAAM and HF-WAAM, and to evaluate the effects of torch mounting configurations and work area placement on vibration levels. The results indicate that torch orientation and the robot's work area significantly influence the vibration experienced during the HF-WAAM process, which in turn affects part quality. The study provides valuable insights into refining the HF-WAAM process for industrial applications, ensuring high-quality part production.

1. Introduction

The Wire Arc Additive Manufacturing (WAAM) process is an additive manufacturing technique that allows large volume of metallic material to be deposited layer by layer to form a part [1,2]. This process allows a part to be manufactured faster than other additive manufacturing processes such as Electron Beam Additive Manufacturing (EBAM) [3,4] or Laser Powder Bed Fusion (LPBF) [5,6]. However, parts manufactured by WAAM have low dimensional and geometric accuracy [7,8].

Like any other metal additive manufacturing process, WAAM produces parts with internal and external defects, such as porosity [9], voids [10], inclusion, crack [11], burn-through, undercutting, spatter, collapse, unmelted wire, delamination, uneven bead height [12], geometric [13]. The presence of these defects decreases the component mechanical properties and, in some cases, makes their use in service unfeasible [14]. To reduce the negative effects of the defects formed, the use of forging during the additive manufacturing process has been successfully proposed. Three variants of additive manufacturing processes with forging have been proposed namely High Pressure Interpass Cold Rolling (HPICR) [15], Hot Micro-Rolling (HMR) [16], and Hot Forging WAAM (HF-WAAM) [17]. The last variant stands out favorably in relation to the others because forging occurs simultaneously with the deposition of material, requiring no downtime for cooling the deposited material nor for carrying out the forging operation, presenting greater flexibility of adaptation to the parts produced (enabling the manufacture of parts of greater geometric complexity) and requiring lower forging loads than the other variants (typically below 100 N) [18].

HF-WAAM is a process that uses a hammer placed inside the shielding gas nozzle to hot forge the deposited material in the visco-plastic state, i.e., at temperatures where solid state transformation induced by simultaneous imposition of deformation and temperature can occur. This hammer is driven by a pneumatic actuator that controls the movement of the hammer to forge the material immediately after its deposition [19].

The WAAM process makes use of automatic systems such as industrial robots [20,21] or Computer Numerical Control (CNC) machines [22,23] to move the welding torch. Thus, this process can operate continuously for several hours or days until a part is produced.

---

* Corresponding author at: UNIDEMI, Department of Mechanical and Industrial Engineering, NOVA School of Science and Technology, Universidade NOVA de Lisboa, 2829-516 Caparica, Portugal.

E-mail address: nam.mendes@fct.unl.pt (N. Mendes).

https://doi.org/10.1016/j.measurement.2024.116576
Received 13 September 2024; Received in revised form 2 December 2024; Accepted 20 December 2024
Available online 24 December 2024
0263-2241/© 2024 The Authors. Published by Elsevier Ltd. This is an open access article under the CC BY license (http://creativecommons.org/licenses/by/4.0/).

Automatic handling systems ensure that the WAAM process is repeatable and allows the production of parts with complex geometries without the use of supports to hold the part in place [24]. The ability to eliminate support structures is crucial to the advancement of this technology, as it substantially reduces the production time of a part. This results from reducing the amount of material deposited and eliminating additional post-processing steps to remove the support. Another benefit of this typology is the reduction of material waste.

It is expected that the use of an industrial robot in the realization of the HF-WAAM process will bring to this process all the advantages listed above for the WAAM process and also the possibility of manufacturing parts of complex geometry whose path made by the welding torch occurs in three-dimensional space by varying the position of the tool (x, y, z) and its orientation (Rx, Ry, Rz) [25,26].

In the HF-WAAM process, a hammer forges the just deposited material to form a flatter surface, which can be the final surface of the part or the surface of a layer of material that makes up the part. To achieve good dimensional accuracy in the final part, it is important for the hammer to strike the deposited material parallel to a plane that encompasses one of the part's final surfaces (such as the top surface). This approach helps prevent deformities, excess material deposition, and facilitating the deposition of molten material to form upper layers of the part.

The integration of forging with WAAM processes has shown considerable advancements in the quality of produced parts. Sokolov et al. [27] demonstrated that combining metal additive manufacturing with hot rolling reduced residual porosity and refined the microstructure, leading to enhanced tensile strength and elongation. Similarly, Duarte et al. [17] developed an innovative WAAM system with in-situ hot forging that decreased porosity and improved mechanical properties through localized high-temperature plastic deformation. Zhang et al. [28] highlighted that compression of Ti–6Al–4 V deposited by LPBF could decrease porosity by up to 75 % and improve microstructure homogeneity. Fang et al. [29] reported that WAAM samples with interlayer hammering exhibited increased yield strength (from 148.4 MPa to 240.9 MPa) and ultimate tensile strength (from 288.6 MPa to 334.6 MPa), alongside significant grain refinement due to continuous deformation and heat treatment. Ma et al. [30] observed graded microstructural evolution in Ti–6Al–4 V samples, which influenced the mechanical properties, revealing higher tensile strength in bonding zones.

Colegrove et al. [31] emphasized that rolling WAAM steel parts could reduce distortion and residual stresses while enhancing grain refinement. Hopper et al. [32] showed that the combination of hot forging and heat treatment improved the mechanical consistency of AM 316L stainless steel parts by reducing porosity and creating a robust microstructure. Meng et al. [33] utilized an electro-assisted micro-forging technique that effectively decreased porosity and simultaneously enhanced strength and ductility in Ti6Al4V samples, revealing mechanisms that healed defects while controlling microstructure coarsening. Xiong et al. [34] proposed a hammering-assisted hybrid WAAM process that significantly refined grain size, optimized strength, and reduced texture anisotropy, finding that a hammering temperature of 850 °C with 40 % deformation yielded the best results. Xiong et al. [35] further elaborated on the benefits of using a spherical hammer head for hot hammering, showing an average grain size reduction from 361 μm to 62 μm and improved yield strength due to combined recrystallization and crystallization effects.

Hönnige et al. [36] discussed machine hammer peening as an alternative to rolling, which refined the microstructure and reduced residual stress in WAAM Ti-6Al-4 V walls. Saremi et al. [37] reported that hot forging of Inconel 718 could minimize defects and achieve dynamic recrystallization, leading to a fine, isotropic microstructure. Xiong et al. [38] investigated a trailing hammer peening technique in WAAM that improved surface hardness by 21.6 % and increased tensile strength from 560.8 MPa to 661.9 MPa, highlighting the benefits of grain refinement and induced dislocation density. Collectively, these studies underscore that forging techniques, whether applied in-situ or as post-treatment, can significantly enhance the structural integrity, reduce porosity, and improve the mechanical performance of WAAM-manufactured components.

The continuous hitting of the hammer on the deposited material at a given frequency generates vibrations in the equipment that performs the HF-WAAM process. This vibration will be more impactful in less rigid equipment and may affect the HF-WAAM process and the part to be manufactured. For example, the path described by the tool (welding torch and hammer) can be affected by vibration causing the tool to deviate from the desired path. Vibration is characterized by amplitude and frequency, while amplitude is related to the intensity of the loads that cause the vibration, frequency identifies the periodicity with which the vibration occurs allowing the identification of various problems with industrial equipment, namely industrial robots [39].

Vibration poses some challenges to industrial processes performed by robots such as machining [40,41], deburring [42,43], and friction stir welding (FSW) [44,45]. In any of these industrial processes, vibration combined with high loads jeopardize the potential applicability of the process. Therefore, these processes require sensorial systems that allow assisting the industrial robots in the execution of their paths, making the real paths executed by the robots closer or equal to the ideal/desired paths [46–48]. The machining [49,50] and deburring [42,51] processes exhibit high frequency and low amplitude vibrations in the face of medium intensity loads generated in the process, while FSW process exhibits low frequency and low amplitude vibrations in the face of high process loads [52,53]. On the other hand, the HF-WAAM process exhibits low intensity loads and medium frequency vibrations, thus differing from the previous processes [54].

The aim of this study is to develop and evaluate a novel robotic cell tailored for HF-WAAM. The research seeks to establish the process parameters for HF-WAAM and assess the feasibility of using a low-payload industrial robot to produce high-quality parts. Additionally, the study aims to investigate the impact of robot-induced vibrations on the manufacturing process and determine the effects of torch orientation and work area placement on the quality of the produced parts.

2. Additive manufacturing robotic cell

To achieve the objectives of this study, a robotic cell was built to perform the HF-WAAM and WAAM processes. The robotic cell was divided into three subsystems, i.e., the HF-WAAM torch, the torch movement and WAAM process generation subsystem, and the HF-WAAM process drive subsystem. In addition, this robotic system was instrumented with accelerometer sensors to measure vibration in the robot and the HF-WAAM torch to assess the extent to which vibration affects the part manufacturing process. The vibration was also evaluated with a redundant vision system using a high-speed camera for term comparison and data validation.

2.1. Wire arc additive manufacturing torch

A HF-WAAM torch was developed and built focusing on improving the HF-WAAM torch proposed in [54]. With the successive use of the torch proposed in the previous study, several operating problems were identified, namely instability of the moving parts associated with the movement of the forging hammer; problems of electrical insulation of the hammer; and difficulties in changing the wire both in the routing of the wire inside the torch and too high resistance to move the handle that fixes the wire to the pulley mounted on the motor shaft.

The torch developed is schematically represented in Fig. 1 and its composing elements are identified in Table 1. Two pneumatic cylinders (14), a linear guide (18), a spring (5), a stepper motor (6), a 10 kΩ electrical resistance (21), seven pneumatic fittings, a bearing (8), a motor shaft coupling (7), a custom hammer (20), and several custom-

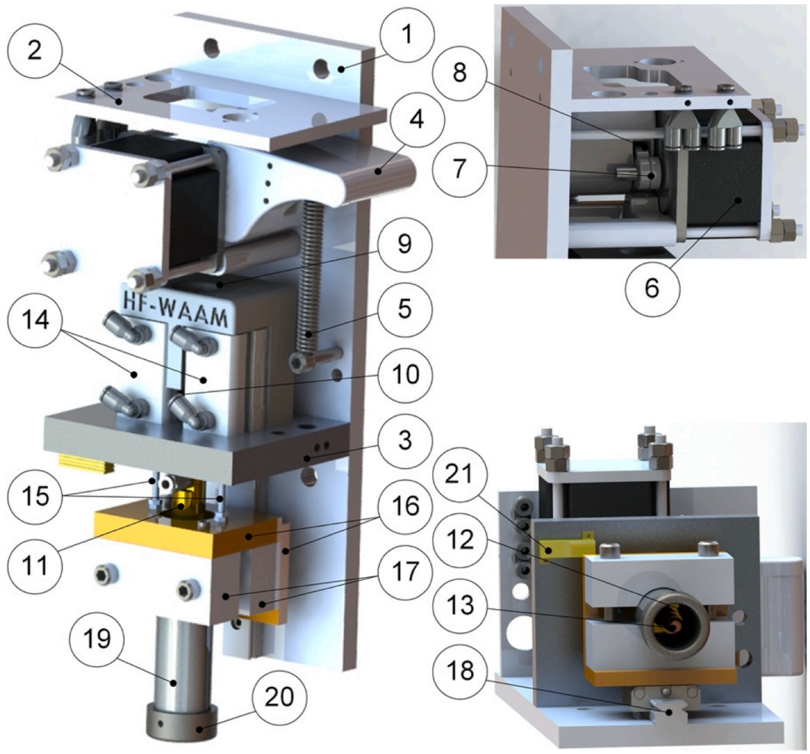

Fig. 1. HF-WAAM torch represented in computer aided design (CAD) drawing.

Table 1
List of constituent components of the HF-WAAM torch. Dimensions not represented in the Description column are in mm.

Component	Description	Qt.	Identification
Back plate	10 mm thick aluminum plate	1	1
Upper cross plate	6 mm thick aluminum plate	1	2
Lower cross plate	10 mm thick aluminum plate	1	3
Lever	Polylactide (PLA)	1	4
Spring	Steel	1	5
Stepper motor	RS PRO 2.5 V, 1.26 Nm	1	6
Pulley	∅ext 15	1	7
Bearing	∅int 6.35 × ∅ext 15	1	8
Primary wire guide	∅int 8	1	9
Secondary wire guide	∅int 6	1	10
Nozzle support	∅int 4	1	11
Welding diffusor	∅int 1.2	1	12
Welding nozzle	∅int 1	1	13
Pneumatic cylinder	∅12 × 10	2	14
Spindle	∅ 3	2	15
Bakelite plate	Bakelite	2	16
Ring nozzle	Stainless steel	1	17
Linear guide and carriage	24 × 16	1	18
Spacer	∅int 6 × ∅ext 8	1	19
Hammer	∅int 25 × ∅ext 35	1	20
Electric resistance	10 kΩ − 25 W	1	21

made mechanical parts were used in the construction of this torch.

Three modifications were made to the torch to facilitate the wire change. One of the modifications was to increase the length of the lever (4) by 15 mm, leading to an increase in the effort arm and a decrease in the force required to move the lever (4). In addition, the length of the upper cross plate 2 was increased by 20 mm so that the user could rest his/her fingers on this plate while operating the lever (4), performing the wire change operation with less effort. The second modification involved replacing the spring (5) with another one that has a lower elastic constant, thus needing less force to move the lever (4). The third modification concerns the introduction of a new part, a secondary wire guide (10), between the primary wire guide (9) and nozzle support (11) to facilitate the entry of the wire into the nozzle support (11).

A bakelite plate 16 was introduced between the carriage of the linear guide (18) and the ring nozzle (17) to allow the up-and-down motion of the forging hammer (20) and improve the electrical insulation and stiffness. For the same purpose, another bakelite plate 16 was introduced between the ring nozzle (17) and the spindles (15). In addition to the introduction of the bakelite plates 16, the distance between the wire and the back plate 1 was increased. The distance from the back of the ring nozzle (17) to the hole was increased by 10 mm, forcing all components that guide the wire to move forward by 10 mm, readjusting the entire torch design.

2.2. Torch movement and wire arc additive manufacturing process generation subsystem (Main hardware)

To perform the HF-WAAM process, it is necessary to move the HF-WAAM torch along the layers of the part depositing filler material. Considering the objective of manufacturing highly complex parts, it is imperative that the equipment maneuvering the torch allows movement in the three spatial directions (X, Y, Z) and in the three orientation directions (Rx, Ry, Rz). For this purpose, we used a KUKA KR6 industrial robot of 6 Degrees of freedom (DoF) and a payload capacity of 6 kg. An OERLIKON CITOWAVE 520 welding machine, employing the Gas Metal Arc Welding (GMAW) variant, was used to generate and control the electric arc during the execution of the HF-WAAM process. Thus, the filler material is properly melted and deposited, and the desired part is built. To support the parts manufactured by HF-WAAM during their construction, a table and a support base were also used. They ensure the correct positioning of a substrate, on which the part is built, and ensure that it does not move during the process. In addition, the table and the support base withstand the impact resulting from forging. The robotic cell is depicted in Fig. 2.

2.3. Wire arc additive manufacturing process drive subsystem

To control the WAAM and HF-WAAM processes, a process drive

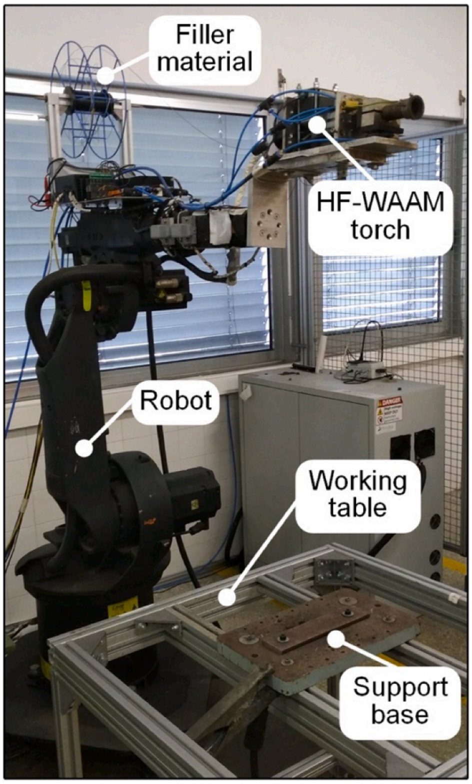

Fig. 2. Robotic cell to perform the HF-WAAM process.

subsystem was incorporated between the industrial robot and the torch. This subsystem is used to control the forging hammer, electric arc, shielding gas and wire feed rate. A microcontroller, Arduino UNO, was introduced between the industrial robot and each respective actuator. The robot is responsible for controlling the system's four triggers while the Arduino interfaces all the hardware elements. A 5/2-way bi-stable solenoid pneumatic valve and two solid state relays were used to actuate the two pneumatic cylinders in the torch and consequently the forging hammer. To control the ignition of the electric arc, an electric digital output from the Arduino was connected to the welding machine. The shielding gas was regulated by a manual flow regulator and actuated by a 2/2-way single-stable solenoid pneumatic valve. A stepper motor driver TB6600 was introduced between the Arduino and the stepper motor to control wire feed rate. In addition, a push-button panel was added to the subsystem to serve as a user interface and allow the user to perform safety instructions and manually control wire feed rate when the system is off. A schematic representation of this subsystem is shown in Fig. 3.

2.4. Vibration acquisition system

The forging stage of material can produce high vibrations in the torch and robot, potentially affecting the system's operation and the quality of part construction. To investigate this issue, a vibration measurement and acquisition system was incorporated in the robotic cell, and the data collected was correlated with the geometry of the built part and with eventual abnormal events to the functioning of the robotic cell.

The vibration acquisition system is composed by an Arduino UNO (independent of the previous referred Arduino), four accelerometers MPU6050 and a computer. The accelerometers were placed on the robot and the HF-WAAM torch as shown in Fig. 4. Accelerometers 2 and 3 are positioned in close proximity, just 100 mm apart, and rotated 90° for the purpose of data verification. The data acquisition rate used was 21 Hz, the maximum rate imposed by the USB 2.0 communication protocol used, the size of the data messages, and the communication speed allowed by the hardware. The accelerometers used have an accuracy of

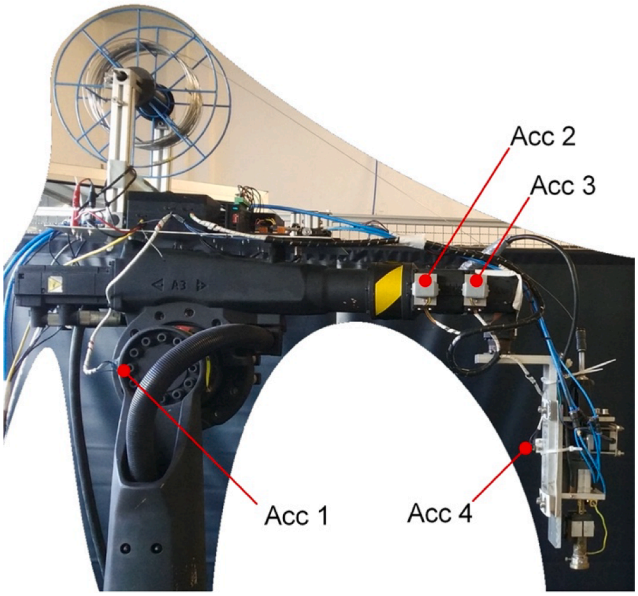

Fig. 4. Vibration acquisition system and placement of the four accelerometers on the robotic cell. Acc 1 – Accelerometer 1, Acc 2 – Accelerometer 2, Acc 3 – Accelerometer 3, and Acc 4 – Accelerometer 4.

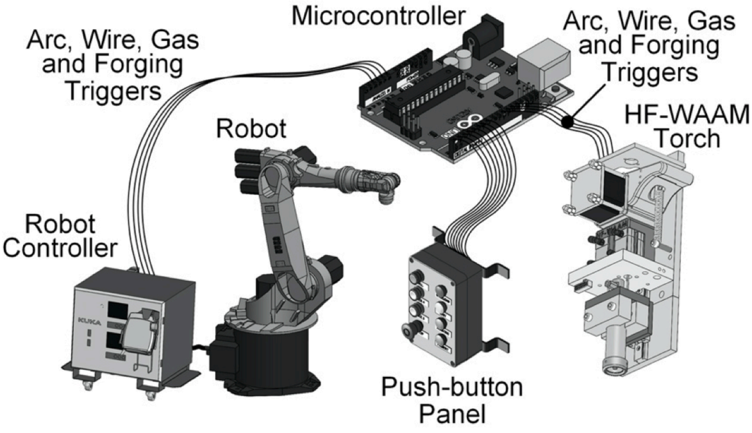

Fig. 3. Schematic representation of the HF-WAAM process drive subsystem.

$\pm$ 0.05 g (where 1 $g = 9{,}81$ m/s^2), ensuring reliable and precise measurements of the vibrations during the experiment.

The data captured by this vibration acquisition system consists of acceleration values of the torch vibration motion. The vibration data underwent processing, with the first step involving the removal of gravity acceleration. Subsequently, in the second step, the system identified the maximum vibration peaks. In a third step, the median of the maximum acceleration values of the torch vibration motion was calculated, using a 1 % sample of the maximum values. This data sample was employed due to the presence of significant noise in the dataset, effectively attenuating the impact of the noise. The median of the maximum acceleration values served as a metric for comparing test results.

A second vibration measurement system was built with a high-speed camera, Photron Mini WX50, and an optical lens Shneider EMERALD 4.0/80F. This vision system was employed to measure torch vibration during the forging stage, and the gathered data was compared with data collected from accelerometer 4. This comparison allowed data produced by the accelerometers $\overrightarrow{a}$ to be validated by the double derivate of position data $\overrightarrow{r}$, extracted from data collected by the vision system, with respect to time using equation (1).

$$\overrightarrow{a} = \frac{\partial(\partial\overrightarrow{r})}{\partial t^2} \tag{1}$$

The vision system operates as follows: the high-speed camera is connected to a computer that stores images, each with a size of 512 × 256 pixels, at an acquisition rate of 10,000 Hz; the captured images show the vibration movement of a given point on the torch back plate, which is solid with accelerometer 4, during the forging execution; to highlight the point of the back plate visualized by the camera, a label was glued on the back plate to contrast with the torch and the background, thus facilitating the identification of the point of interest on the image; the acquired images were processed by purpose-built software to extract the position data $\overrightarrow{r} = (x, y, z)$ of the label over time. The vision system has an accuracy of ± 0.1 mm, ensuring precise measurement of the torch vibration.

3. Experiments

3.1. WAAM and HF-WAAM tests

To test the HF-WAAM robotic cell and find the HF-WAAM process parameters that allow the cell to manufacture high quality parts, test samples were produced in the form of linear walls. The samples were formed by depositing filler material on a steel substrate, which was bolted to the base of the table. The substrate used measured 230 × 60 × 8 mm^3. Each sample comprises 8 layers of ER316LSi stainless steel, with the wall length measuring 150 mm. Initially, the WAAM process was employed to check and fine-tune the parameters that had been previously optimized in earlier studies [17,55] for creating high-quality parts. These refined parameters were then applied to the HF-WAAM process, where additional forging-related parameters were adjusted to further enhance the quality of the forged samples. During the HF-WAAM process for sample production, the first two layers were built using the conventional WAAM process, while the subsequent six layers were forged using HF-WAAM.

No forging was used in the first two layers of the samples to prevent the newly deposited filler material from spreading out on the substrate due to the rapid solidification caused by the cooler temperature of the part, which has a higher heat dissipation area compared to the subsequent layers. Additionally, the hammer ring strikes not only the freshly deposited material but also the colder substrate, which provides less damping, resulting in increased vibrations in the freshly deposited material and consequently hindering the bonding between the deposited material and the substrate.

The feed wire used was 1 mm in diameter and its chemical composition is shown in Table 2. The shielding gas used was Argon 99.99 %. The process parameters wire feed speed (WFS), voltage, current, travel speed (TS), gas flow rate (GFR), welding control mode, forging frequency, pneumatic cylinder pressure, distance to arc center (DAC − distance between the center of the wire and the middle diameter of the hammer) and contact tip to work distance (CTWD − distance between the end of the contact tip and the base material) were used to produce the samples, as shown in Table 3.

There is a rationale behind the selection of parameters in the HF-WAAM process to achieve high-quality parts. Increasing the pneumatic cylinder pressure raises the forging pressure, enhancing the deformation of the deposited layer. This enhanced deformation improves the mechanical properties of the part and reduces porosity. Furthermore, increasing the forging frequency reduces the forged area per stroke, resulting in higher stress applied to the material, which further promotes the deformation of the deposited layer. These carefully adjusted parameters are essential for improving material consolidation and ensuring the production of high-quality parts.

3.2. Robot path for part manufacturing

To make a linear wall, the direction of material deposition was changed between layers using a zig-zag strategy. It started from left to right, and then went from right to left, as shown in Fig. 5. Between the deposition of two consecutive layers, a dwell time of 30 s was consistently maintained to ensure that the freshly deposited layer was adequately solidified. This dwell time was crucial for preventing thermal accumulation that could lead to excessive heat build-up and residual stresses, which may compromise the structural integrity and dimensional accuracy of the final part. By allowing the deposited material to solidify properly, the risk of defects such as warping, incomplete fusion, and distortion was minimized, leading to improved bonding between layers and better overall quality of the manufactured component.

Since forging was applied during the HF-WAAM process, the part under construction and, in particular, the newly deposited layer underwent a size reduction in the forging direction. The hammer's position during the forging process was always higher than the deposited layer, ensuring that the material experienced consistent deformation, as demonstrated in [54]. To maintain a uniform 10 mm gap between the tip of the wire and the previously deposited layer during material deposition, the robot was programmed with one layer at a time in mind. A 10 mm thick Gauge Checker was used to establish this distance, with the hammer positioned in its retracted state. The Gauge Checker was placed between the surface of the retracted hammer (defining a plane) and the highest point of the last deposited layer, ensuring precise and consistent measurement of the gap.

The distances between the hammer and the previously deposited layer were defined for each individual layer to account for variations in height due to the layer's distance from the substrate. Layers deposited and forged closer to the substrate could have different heights compared to those farther away. However, once these distances were determined for a single part, they remained consistent and could be directly reused for the production of identical parts. This method eliminated the need for readjustments while ensuring stable and uniform forging throughout the process.

3.3. Vibration tests

To study the influence of the distance between the area where a part is constructed and the robot base, three work areas were defined for part construction using HF-WAAM. One of the work areas was positioned 1000 mm from the robot base (centered on the first robot joint), while the other two were situated at distances of 1250 mm and 1500 mm from the robot base, respectively. This distance was measured along the x-axis

Table 2
Chemical composition of ER316LSi filler wire (wt. %).

Element	C	Mn	Si	S	P	Cr	Ni	Mo	Cu
wt. %	0.03	1.0—2.5	0.65—1.0	0.03	0.03	18.0—20.0	11.0—14.0	2.0—3.0	0.75

Table 3
WAAM and HF-WAAM process parameters.

Test no.	WFS (m/min)	Voltage (V)	Current (A)	Welding control mode	GFR (l/min)	TS (mm/s)	CTWD (mm)	DAC (mm)	Pneumatic pressure (bar)	Forging frequency (Hz)
T1	4	19	120	Normal	25	7	8	–	–	–
T2	3	19	98–120	Synergic	25	7	10	–	–	–
T3	3	19	98–120	Synergic	20	6	10	–	–	–
T4	3	19	98–120	Synergic	15	6	10	–	–	–
T5	3	19	98–120	Synergic	15	6	10	10	4	8
T6	3	19	98–120	Synergic	15	6	10	15	2.5	8

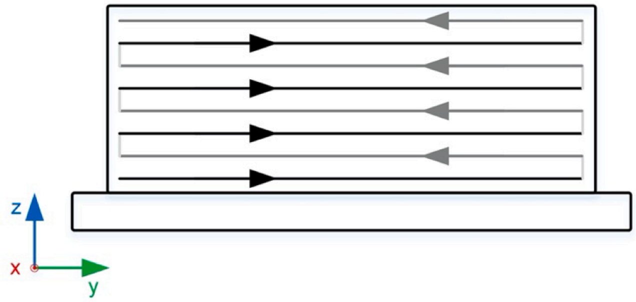

Fig. 5. Zig-zag strategy used in material deposition.

direction in the robot's base referential, remaining constant throughout the part's construction. Fig. 6 depicts the three work areas (P1, P2 and P3) within the robot's domain designated for part construction.

Two ways of mounting the HF-WAAM torch to the robot were studied. In one way, the torch was mounted perpendicularly to the robot flange (perpendicular torch mounting – PTM), as shown in Fig. 6. In the other, the torch was mounted on a bracket along an axis parallel to the robot flange axis (axial torch mounting – ATM), as shown in Fig. 7. PTM and ATM are the two most common tool mounting configurations used in industrial robots. This study aimed to determine whether the type of mounting configuration impacts the HF-WAAM process.

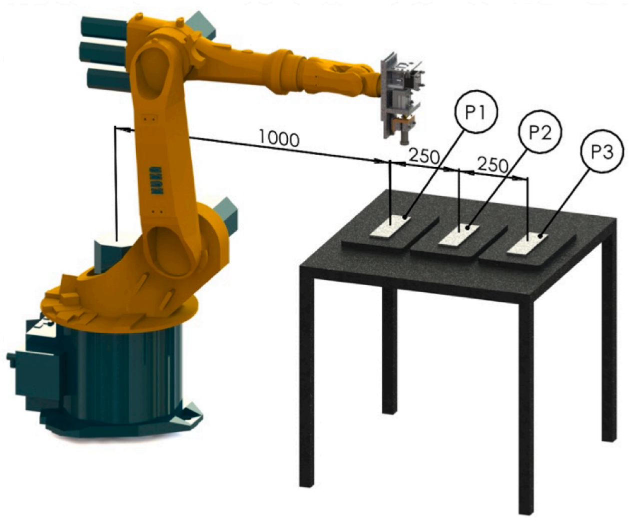

Fig. 6. The three work areas used for part construction. P1, P2 and P3 are work areas 1, 2 and 3, respectively. The torch is mounted perpendicularly to the robot flange (perpendicular torch mounting – PTM).

In order to study how the quality of the parts produced by HF-WAAM is affected by the way the torch is mounted on the robot and the type of work area (WA) used, six tests were carried out crossing the variables shown in Table 4. Each test was repeated 10 times to ensure the repeatability and reliability of the obtained results. This level of repetition was critical for validating the consistency of the data, assessed through measurements using the accelerometers and the vision system. This approach provided comprehensive insights into the dynamic behavior and quality stability of the production process.

3.4. Evaluation of top surface Waviness, geometry and porosity

To ensure the quality and reliability of the HF-WAAM process, the produced samples were thoroughly evaluated in terms of top surface waviness, geometry, and porosity. The evaluation of the produced samples focused exclusively on the effective zone of the part, excluding the first 5 mm and the last 5 mm of the part, as recommended in [56]. This exclusion is justified by the fact that the initial and final regions of the part are prone to the formation of a higher number of defects, which could otherwise bias the results.

3.4.1. Top Surface Waviness

The waviness of the top surface was measured using a Mitutoyo Digimatic Dial Indicator 2046S. The measurement focused on the average waviness (Wa) parameter, which quantifies the mean deviation of the surface profile over a given length. This parameter was chosen to characterize the overall smoothness of the top layer, providing insights into the deposition consistency and quality of the final layer.

3.4.2. Geometry Evaluation

The geometry of the top surface was evaluated by calculating the missing area (A_{miss}) between the actual surface of the fabricated part and the ideal surface of a perfectly prismatic structure. The calculation of this area is performed based on measurements taken with the Mitutoyo Digimatic Dial Indicator 2046S. This method provides a precise quantification of geometric deviations, allowing us to assess any material displacement, deformation, or inaccuracies during the manufacturing process. An example of the calculated missing area is illustrated in Fig. 8, highlighting the deviations from the ideal geometry.

3.4.3. Porosity Analysis

Porosity was assessed qualitatively through visual inspection of the top surface. The number and dimensions of visible pores were examined and recorded to evaluate surface defects. The porosity was classified into four categories: No Visible Porosity (no pores visible to the naked eye on the surface), Low Porosity (few and small visible pores, with minimal impact on surface quality), Moderate Porosity (noticeable pores of

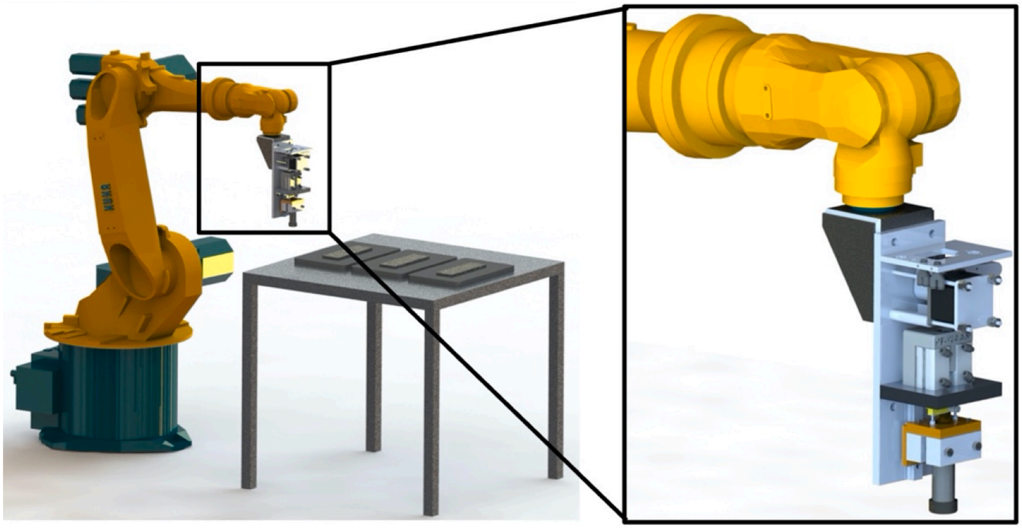

Fig. 7. HF-WAAM torch mounted on a bracket along an axis parallel to the robot flange axis (axial torch mounting – ATM).

Table 4
HF-WAAM tests varying the work area and torch mount type. The test abbreviations are used to identify the type of test.

Torch mounting	Work area		
	P1	P2	P3
Perpendicular	PTM_P1	PTM_P2	PTM_P3
Axial	ATM_P1	ATM_P2	ATM_P3

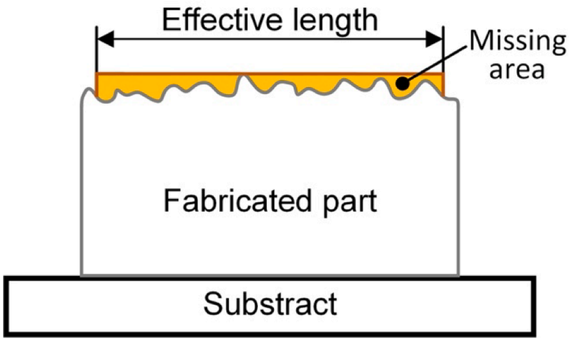

Fig. 8. Schematic representation of the geometric evaluation process, illustrating the method used to calculate the missing area (A_{miss}) between the actual surface of the fabricated part and the ideal surface of a perfectly prismatic structure.

varying sizes, scattered across the surface), and High Porosity (large and/or dense clusters of pores, significantly affecting surface integrity).

4. Test results and discussion

4.1. Test results for process parameterization

The samples produced with the parameters identified in Table 3 are shown in Table 5, while the evaluation of the top surface of these samples is detailed in Table 6. The first four tests (T1, T2, T3, and T4) were carried out using the WAAM process to establish the parameters necessary for manufacturing high-quality samples, which had approximate dimensions of 150 × 4.8 × 11.1 mm^3.

Sample T1 failed during fabrication, as exhibited an insufficient amount of filler material in the left central area, alongside the presence of copper in the right area of the final layer — a clear indication that the

Table 5
Test results of samples produced using the parameters identified in Table 3.

Test no.	Sample
T1	
T2	
T3	
T4	
T5	
T6	

Table 6
Evaluation of the top surface of samples produced using the parameters identified in Table 3. *Sample T1 failed during fabrication, clearly reflecting the inadequacy of the parameters used. Due to the extremely poor outcome, it was not considered for top surface evaluation.

Test no.	Wa (mm)	A_{miss} (mm^2)	Porosity
T1	*	*	*
T2	2.57	527.85	High
T3	1.16	342.68	High
T4	0.34	137.53	No Visible
T5	0.83	253.42	Low
T6	0.28	94.72	No Visible

welding nozzle had melted during the process. Notably, the WFS parameter was set at a high value, while the CTWD remained low. Due to the failure during fabrication, sample T1 was not evaluated further. Subsequent adjustments to these parameters were implemented in the production of sample T2.

Sample T2 revealed the occurrence of humping phenomenon, marked by a high TS. This phenomenon led to the drag of the melt pool along with the material, resulting in the formation of humps within the bead at regular intervals during the WAAM process. Additionally, this sample exhibited high porosity, attributed to an excess of shielding gas. The Wa of T2 was measured at 2.57 mm, and the A_{miss} was 527.85 mm^2, indicating poor surface quality and geometric accuracy.

During the production of sample T3, adjustments were made by reducing the parameters of TS and GFR. Although improvements were observed, the presence of high porosity in sample T3 indicated an excessive amount of shielding gas. The Wa of T3 was 1.16 mm, while the A_{miss} was reduced to 342.68 mm^2, showing significant improvement compared to T2.

Subsequently, the GFR parameter was further reduced to create sample T4. Remarkably, sample T4 exhibited a smooth surface with no visible porosity or excessive deformation, leading to the establishment of the WAAM parameterization. The Wa of T4 was 0.34 mm, and the A_{miss} was further reduced to 137.53 mm^2, demonstrating excellent surface and geometric quality for WAAM-produced samples.

Forging was employed for fabricating samples T5 and T6 to assess the dynamic load tolerance of the robot while simultaneously enhancing the quality of the produced samples, which had approximate dimensions of 150 × 4.8 × 9.4 mm^3.

Sample T5 exhibited irregularities on the forged surface, attributed to the forging hammer being in close proximity to the melting pool — indicating a potential issue with the DAC being too small. Moreover, a deficiency of filler material in the final layer deposition resulted from a robot path correction error, induced by forging forces exceeding the robot's capacity. The sample showed low porosity. The Wa of T5 was measured at 0.83 mm, and the A_{miss} was 253.42 mm^2, reflecting moderate improvement compared to WAAM-produced samples.

In the production of sample T6, adjustments were made by increasing the DAC to 15 mm and decreasing the pneumatic cylinder pressure to 2.5 bar. As a result, sample T6 displayed a consistently forged surface without deviations or material gaps, with no visible porosity. The increase in DAC and reduction in pneumatic cylinder pressure effectively mitigated the loads transmitted to the robot, enabling it to operate without deviating from its trajectory. These parameters were established based on thermographic images of the WAAM process, where both the melt pool and the surrounding temperatures were monitored, as well as from the procedure described in our previous study [18]. The Wa of T6 was the lowest among all samples, at 0.28 mm, and the A_{miss} was 94.72 mm^2, demonstrating superior surface and geometric quality.

Comparing sample T4 made by WAAM with sample T6 made by HF-WAAM, it can be observed that their geometrical characteristics are very similar. Both samples have the same shape and a similar size, and the edges of the samples are smooth, indicating that the manufacturing processes used were successful in producing consistent results. Additionally, sample T6 outperformed T4 in terms of both average waviness (0.28 mm vs. 0.34 mm), missing area (94.72 mm^2 vs. 137.53 mm^2), and porosity (no visible porosity in both cases). These findings highlight the benefits of HF-WAAM in producing parts with enhanced quality. Overall, these findings demonstrate that HF-WAAM can achieve comparable or superior results to WAAM, with improved surface finish, geometric accuracy, and reduced porosity. The refined parameters used to produce sample T6 proved to be the most suitable for the HF-WAAM process within the robotic cell and were subsequently applied for conducting vibration tests.

4.2. Test results for the influence of vibration on the HF-WAAM process

4.2.1. Tests performed with the HF-WAAM torch mounted parallel to the robot flange axis – ATM

To study the influence of the torch mounting on the robot and the distance between the robot base and the WA used to build parts, six tests were performed as described in section 3. The vibration caused by the forging operation was monitored during the HF-WAAM process in the construction of parts with a linear wall shape. Fig. 9 shows the vibration recorded by the four accelerometers during the construction of the third layer (first layer using forging) of the part fabricated with the torch mounted parallel to the robot flange axis – ATM using the P1 WA and the HF-WAAM process parameters used in the T6 test (shown in Table 3). The results of these six tests are presented in Table 7, using the median of the maximum acceleration values as the metric. This metric was employed to mitigate the impact of noise in the acceleration data of the vibration motion, as visible in Fig. 9. The test results were specifically calculated from vibration data obtained during the construction of a complete part.

The vibration recorded by accelerometer 4 is higher than the vibration recorded by any other accelerometer. This is because this accelerometer is located next to the forging hammer and is the farthest of the four accelerometers from the base of the robot. Because the robot is an articulated machine, the end-effector region is less rigid than any other region of the robot. The end-effector region is the region farthest from the robot base (the robot's support point) and consists of weaker links, joints, and motors. On the other hand, the closer you are to the base of the robot, the larger and more robust the links, joints and motors that make up the robot, and therefore the greater the rigidity, as shown by the low vibration values recorded by accelerometer 1. In addition, the joints of the robot allowed the damping of the vibrations, as shown by the vibrations collected by the different accelerometers, for example, between accelerometers 4 and 3. There was a joint between these accelerometers that caused the vibration values recorded by accelerometer 3 to be significantly lower than those recorded by accelerometer 4. In this case, there was a 74 % reduction in the median of the maximum acceleration values when the part was built in P1 WA, as shown in Table 8. This table shows the reduction in vibration along the robot arm from the torch to the base of the robot. Accelerometers 2 and 3 recorded very similar vibration values because they were placed very close to each other on the same link of the robot.

The WA used by the robot to build parts had a large influence on the vibration of the robot and the HF-WAAM torch. When comparing the rows in Table 7, it becomes evident that the P3 WA was the least favorable of the three work areas for performing the HF-WAAM process. In contrast, P1 WA was the most favorable because the vibration recorded on the robot and torch was significantly lower.

This behavior was due to the configuration and positioning of the robot joints which, when the robot was in P1 WA, minimized the extension of the arm compared to the other work areas. As a result, the forces and moments supported by the robot joints were minimized.

Taking as a reference the most unfavorable vibration situation, i.e., the vibration recorded by accelerometer 4 during the test performed in P3 WA, which recorded a median of the maximum acceleration values of

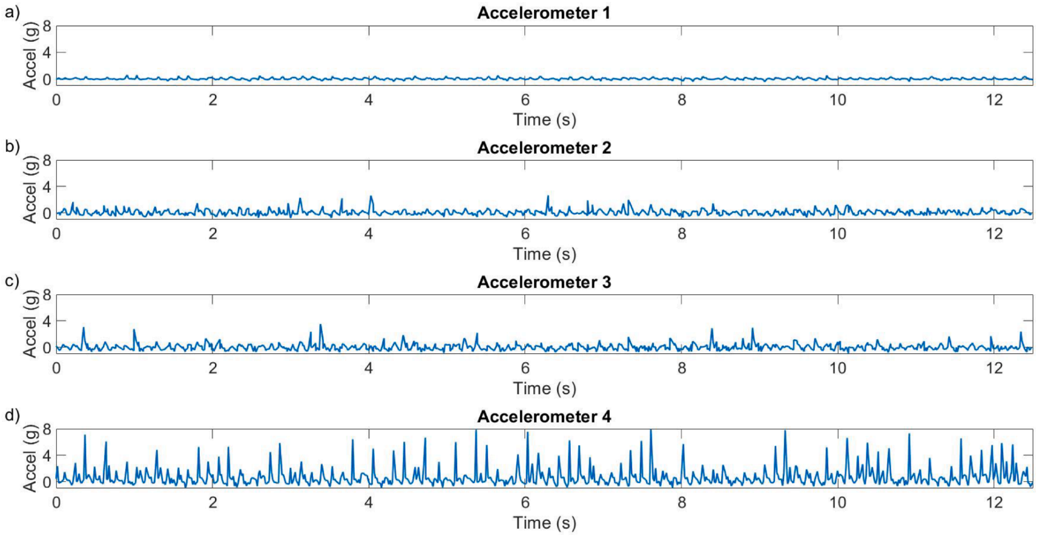

Fig. 9. Vibration recorded by the four accelerometers during the construction of the third layer (first layer using forging) of the part fabricated with the torch mounted parallel to the robot flange axis – ATM using the P3 WA and the HF-WAAM process parameters used in the T6 test (shown in Table 3): a) Accelerometer 1, b) Accelerometer 2, c) Accelerometer 3 and d) Accelerometer 4. The y-axes of the graphs represent acceleration (Accel) in units of 'g' (1 g = 9.81 m/s^2).

Table 7
Median of the maximum acceleration values of the vibration motion resulting from HF-WAAM part-construction tests with the torch mounted parallel to the robot flange axis – ATM, using the three work areas and the HF-WAAM process parameters previously used in the T6 test (shown in Table 3). Vibration recorded by the accelerometers. The vibration is expressed in units of 'g' (1 g = 9.81 m/s^2).

WA	Accelerometer			
	1	2	3	4
P1	0.04 g	0.13 g	0.14 g	0.48 g
P2	0.05 g	0.15 g	0.15 g	0.57 g
P3	0.07 g	0.19 g	0.22 g	0.84 g

Table 8
Decrease in vibration along the robotic arm relative to the region of the robot where the greatest vibration was recorded, i.e., in the torch region (accelerometer 4). These results are derived from the information recorded by the accelerometers.

WA	Accelerometer		
	1	2	3
P1	92 %	72 %	71 %
P2	91 %	74 %	74 %
P3	92 %	78 %	74 %

0.84 g, a decrease in vibration is observed in P1 and P2 work areas with respect to P3, with a decrease of 43 % and 32 % respectively in the median of the maximum acceleration values, as shown in Table 9.

Table 9
Decreased vibration in each region of the robotic arm when using P1 and P2 work areas compared to the vibration recorded in the corresponding robot region when building a part in P3 WA, the one where the highest vibration was recorded. These results are derived from the information recorded by the accelerometers.

WA	Accelerometer			
	1	2	3	4
P1	43 %	28 %	38 %	43 %
P2	25 %	20 %	33 %	32 %

In general, parts produced in P1 WA (ATM_P1) showed better dimensional and geometric accuracy, with the top surfaces exhibiting minimal waviness (Wa = 0.28 mm) and nearly nonexistent local collapse in the final layer, compared to parts produced in work areas farther from the robot base, i.e., P2 (ATM_P2) and P3 (ATM_P3), as shown in Fig. 10 and Table 10. Local collapse in the final layer was qualitatively assessed through visual inspection.

The parts produced in P2 WA (ATM_P2) exhibited some waviness (Wa = 0.44 mm) and small local collapse in the final layer, while the A_{miss} was measured at 148.33 mm^2, indicating moderate geometric deviations. No visible porosity was observed in these parts.

On the other hand, the parts produced in P3 WA (ATM_P3) showed not only higher waviness (Wa = 0.67 mm) and excessive local collapse in the final layer on the tops of the parts but also areas of underfill. These samples had the highest A_{miss} value (201.34 mm^2) and exhibited low porosity, reflecting the poorest dimensional and geometric quality among the three work areas.

These observations lead to the conclusion that the WA used to build the parts significantly affected the final quality of the parts produced. There is a clear relationship between the increasing distance from the robot base and the decreasing dimensional and geometric accuracy, as demonstrated by the increasing Wa and A_{miss} values and the appearance of porosity in parts produced farther from the robot base.

4.2.2. *Tests performed with the HF-WAAM torch mounted perpendicular to the robot flange – PTM*

The second HF-WAAM torch mounting configuration, torch perpendicular to the robot flange – PTM, was tested in part manufacturing. All tests performed with this torch mounting configuration in any of the three work areas failed during the production of the third layer of the part when forging was used. As shown in Table 11, the vibration levels recorded during the manufacture of the parts were very high. During part manufacturing in P1 and P2 work areas, the HF-WAAM process became unstable, leading to arc extinguishment and preventing deposition of the material in the desired way. This event was caused by the high amplitude of the vibrations. When a part was manufactured in P3 WA, the farthest from the robot base, the vibration amplitude and forces were too high for the robot leading it to go into an emergency stop due to exceeding the maximum allowable torque at the joint closest to the torch. This joint was the smallest and least robust joint on the robot and was operating perpendicular to the direction of the forging force. Comparing the vibration recorded by the

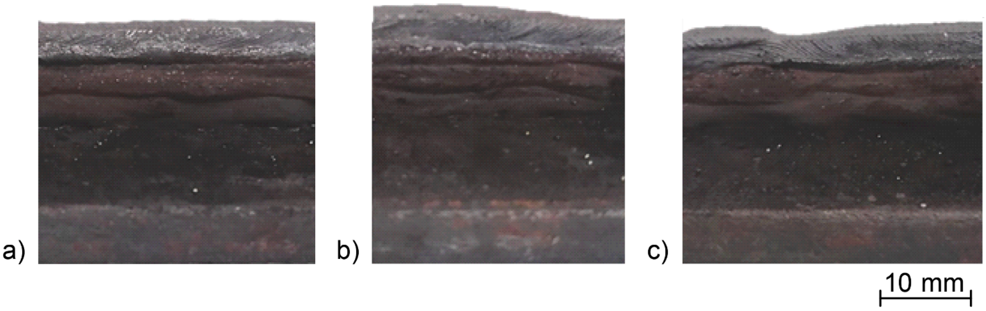

Fig. 10. Forging surface morphology of the parts produced in: a) P1, b) P2 and c) P3 work areas.

Table 10
Evaluation of the top surface of samples produced using the parameters identified in Table 3.

Sample	Wa (mm)	A_{miss} (mm^2)	Porosity
ATM_P1	0.28	94.72	No Visible
ATM_P2	0.44	148.33	No Visible
ATM_P3	0.67	201.34	Low

Table 11
Median of the maximum acceleration values of the vibration motion resulting from HF-WAAM part manufacturing tests with the torch mounted perpendicular to the robot flange – PTM, using the three work areas and the HF-WAAM process parameters previously used in the T6 test (shown in Table 3). Vibration recorded by the accelerometers. The vibration is expressed in units of 'g' (1 $g = 9.81$ m/s^2).

WA	Accelerometer			
	1	2	3	4
P1	0.06 g	0.36 g	0.37 g	0.85 g
P2	0.08 g	0.40 g	0.43 g	0.98 g
P3	0.13 g	0.54 g	0.56 g	1.52 g

accelerometers when using the two torch mounting configurations on the robot flange, shown in Table 12, there was a very significant increase in vibration of the order of 123 % when using the tool mounting perpendicular to the robot flange – PTM. The increased vibration levels in PTM are attributed to differences in force and vibration transfer to the robot, which affected its dynamic load tolerance. Since the tip of the robot arm is less rigid, these vibrations and forces can cause significant deviations from the programmed trajectory, destabilizing the deposition process.

The robot's dynamic load tolerance is critical in HF-WAAM applications, as the forces generated during forging directly impact its path accuracy. If the robot deviates from its intended trajectory, the deposition process becomes unstable, leading to inconsistencies in material deposition and reduced part quality. Based on part manufacturing tests, we can state that the robotic system is not capable of manufacturing parts using HF-WAAM under these conditions.

Similar to previously reported tests using the HF-WAAM torch mounted parallel to the robot flange axis – ATM, tests using the torch mounting configuration perpendicular to the robot flange – PTM revealed that vibration was more severe in work areas farther from the robot base. This increase in vibration can be attributed to the reduced stiffness of the robot arm in extended positions, amplifying cantilever effects and mechanical stresses. Furthermore, robot vibration was observed to be greater at the torch and in regions of the robot closer to the torch, highlighting the sensitivity of these areas to the mechanical forces and vibrations generated during the HF-WAAM process.

Table 12
Increased torch and robot vibration when the torch is mounted perpendicular to the robot flange – PTM versus when the torch is mounted parallel to the robot flange axis – ATM. These results are derived from the information recorded by the accelerometers.

WA	Accelerometer			
	1	2	3	4
P1	48 %	168 %	169 %	78 %
P2	54 %	168 %	190 %	72 %
P3	102 %	191 %	155 %	81 %

4.2.3. *Vibration test results using the vision system*

The vision system was used to capture movement of the torch. The torch was mounted both parallel to the robot flange axis – ATM and perpendicular to the robot flange – PTM. These measurements were taken during part manufacturing by HF-WAAM in the three work areas (P1, P2, and P3), using the HF-WAAM parameters established in the T6 test. Fig. 11 a) illustrates an example of torch movement captured by the vision system across eight hammering operations, while Fig. 11 b) amplifies the details of a specific hammering operation. In this figure, the different regions are defined as follows: Region I illustrates the hammer at rest, in contact with the forged workpiece; Region II portrays the hammer moving away from the workpiece; Region III depicts the hammer at rest, distant from the workpiece; Region IV shows the hammer in motion, approaching the workpiece without contact; and Region V captures the hammer descending to forge the workpiece, causing material deformation. Additionally, Fig. 11 b) illustrates a position data adjustment curve generated from vision system recordings, enhancing accuracy by correcting variations and errors, thereby providing a refined representation of real-time movement or location.

Figs. 12 and 13 a) depict the velocity and acceleration of the torch vibration movement during a hammering operation, respectively. These curves are derived from the first and second derivatives of the adjusted vibration movement curve shown in Fig. 11 b), collected by the vision system. The graph represented in Fig. 13 b) illustrates a hammering operation captured with accelerometer 4. As seen in Fig. 13 b), the data collected by this device, when compared to Fig. 13 a), does not fully depict the acceleration pattern due to a lower data acquisition frequency than that used for the vision system. However, by employing the median comparison metric of the maximum acceleration values and utilizing a large dataset, i.e., data related to the construction of a complete part, the comparative values remain unaffected. Despite the absence of some data in the acceleration pattern captured by accelerometer 4, it can be stated that both acceleration patterns obtained by accelerometer 4 and the vision system exhibit similarities, as evidenced in Fig. 13 a) and b).

The vibration recorded by the vision system was similar to that of accelerometer 4, as shown in Table 13. This result was expected given that the vibration collection performed by the vision system focused on an area close to the location of the accelerometer 4 and exactly on the component on which this accelerometer was placed.

The vibration data collected from both measurement systems consistently revealed that P3 WA exhibited the highest levels of vibration. This finding reaffirmed the sensitivity of this WA to vibration

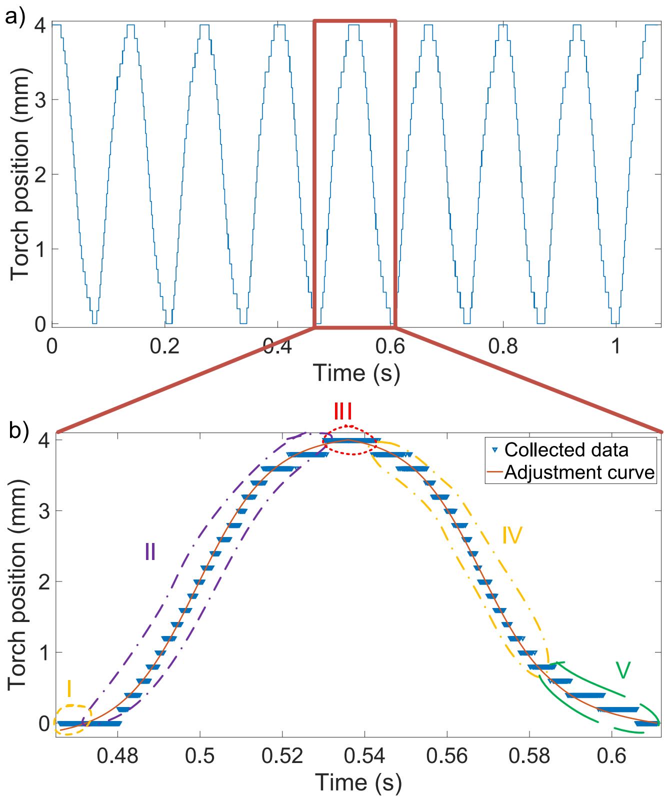

Fig. 11. Illustration of torch movement recorded by the vision system: a) during eight hammering operations; b) amplification of a hammering operation. The torch was mounted parallel to the robot flange axis – ATM, and the WA in use was P2. The different regions are defined as follows: Region I illustrates the hammer at rest, in contact with the forged workpiece; Region II portrays the hammer moving away from the workpiece; Region III depicts the hammer at rest, distant from the workpiece; Region IV shows the hammer in motion, approaching the workpiece without contact; and Region V captures the hammer descending to forge the workpiece, causing material deformation. Additionally, Fig. 11 b) illustrates a position data adjustment curve generated from vision system recordings, enhancing accuracy by correcting variations and errors, thereby providing a refined representation of real-time movement or location.

during the HF-WAAM process. P2 WA exhibited intermediate vibration levels, while P1 consistently demonstrated the lowest vibrations, confirming a consistent trend between the two measurement systems. These findings align with the quality assessment of the parts produced in these work areas, where P1 WA (ATM_P1) showed superior dimensional and geometric accuracy, including the lowest average waviness (Wa = 0.28 mm) and missing area (A_{miss} = 94.72 mm^2) with no visible porosity. In contrast, P3 WA (ATM_P3), which exhibited the highest vibration levels, also displayed the poorest quality, with the highest Wa = 0.67 mm, Amiss = 201.34 mm^2, and the presence of low porosity.

A notable aspect of the current research was the impact of torch orientation on vibration levels. When the torch was mounted parallel to the robot flange axis — ATM, it was evident from the data collected by both measurement systems that vibration levels were notably lower. This orientation also resulted in elevated part quality, as reflected in the low Wa and A_{miss} values for parts produced in this configuration. In contrast, when the torch was mounted perpendicular to the robot flange — PTM, higher vibration levels were observed, correlating with reduced part quality. This demonstrates that torch orientation is a significant factor influencing vibration and, consequently, the final quality within the HF-WAAM process.

It is important to highlight that both vibration measurement systems provided mutually validating results. This mutual validation enhances the overall confidence in the collected vibration data, confirming the consistency of the findings across the different systems. This internal validation of the data adds strength to the research and bolsters the integrity of the collected information.

The results further demonstrate that the robotic cell is capable of producing high-quality parts using the HF-WAAM process, provided that the torch is mounted parallel to the robot flange axis (ATM) and the work area distance from the robot base is less than 1250 mm, as seen in P1 and P2 WA. Under these conditions, vibration levels remain low, and part quality is improved, as evidenced by the superior Wa and A_{miss} values observed in the samples produced in P1 and P2 WA. These findings provide valuable insights for refining the HF-WAAM process, ensuring that the robotic cell can achieve both high-quality parts and reliable process performance when operating within these parameters.

In summary, while there are minor variations in the vibration data attributed to differences in measurement tools, the overall consistency in trends across work areas and the pronounced effect of torch orientation on vibration levels validate the central findings of this research. Furthermore, the quantitative analysis of top surface waviness, geometry, and porosity strongly correlates with the observed vibration trends, emphasizing the importance of minimizing vibration to achieve elevated quality parts. These findings provide valuable insights for refining the HF-WAAM process, leading to enhanced efficiency, reliability, and part quality in additive manufacturing techniques.

5. Conclusions

This study presented the development and evaluation of an innovative robotic cell for the HF-WAAM process. The research established refined parameters for both WAAM and HF-WAAM processes, demonstrating that combining material deposition with hot forging can produce high-quality parts with improved dimensional accuracy, surface

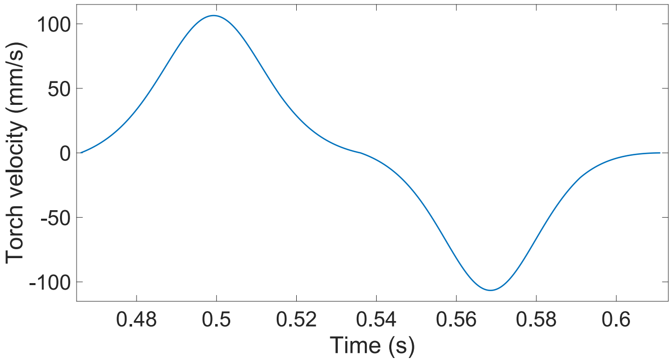

Fig. 12. Illustration of torch movement velocity recorded by the vision system during a hammering operation. The depicted curve was obtained through the derivative of the position data adjustment curve represented in Fig. 11 b).

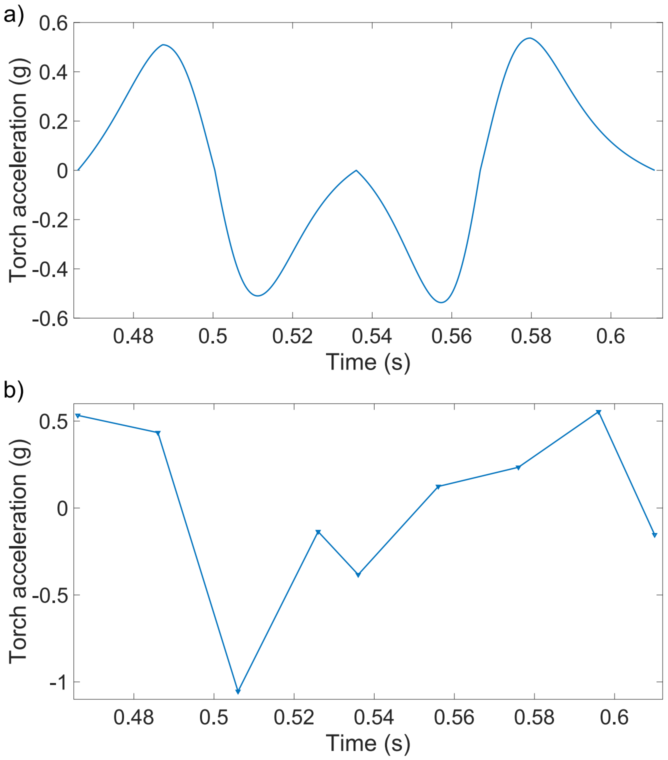

Fig. 13. Illustration of torch movement acceleration recorded by: a) the vision system; b) the accelerometer 4 during a hammering operation. The presented curve in Fig. 13 a) was derived through the double derivative of the position data adjustment curve illustrated in Fig. 11 b).

Table 13
Median of the maximum acceleration values of the vibration motion resulting from HF-WAAM part-construction tests, obtained with the torch mounted parallel to the robot flange axis – ATM and with the torch mounted perpendicular to the robot flange – PTM. These tests were conducted using the same three work areas and HF-WAAM process parameters as those previously used in the T6 test, as shown in Table 3. The vibration is expressed in units of ’g’ (1 g = 9.81 m/s^2). These results are derived from the data recorded by the vision system.

WA	ATM	PTM
P1	0.48 g	0.85 g
P2	0.54 g	0.96 g
P3	0.68 g	1.27 g

uniformity and minimal porosity. Vibration analysis revealed that both torch orientation and the robot’s work area play a critical role in influencing the quality of the manufactured parts. The parallel torch mounting to the robot flange axis (ATM) and the use of work areas closer to the robot base (less than 1250 mm) were found to result in lower vibration levels, which directly contributed to the production of parts with elevated quality, as evidenced by improved top surface waviness (Wa) and missing area (A_{miss}) values.

Furthermore, the cross-validation of vibration data obtained from accelerometers and the vision system confirmed the robustness and consistency of the results. These findings underscore the importance of optimizing both the robot configuration and process parameters to minimize vibration and maximize the efficiency, reliability, and overall quality of the HF-WAAM process in industrial applications. These findings provide valuable recommendations for further improvements and applications of this additive manufacturing process in industrial environments.

The limitations of this study include its focus on the fabrication of relatively simple geometries and single-material parts. Future work will address these limitations by exploring the fabrication of parts with more complex geometries, the use of different materials, and the deposition of parallel beads within the same layer. These aspects, which may be influenced by vibration and the forces exerted on the robot, will be investigated to expand the applicability and robustness of the HF-WAAM process in more demanding manufacturing scenarios.

CRediT authorship contribution statement

Nuno Mendes: Writing – review & editing, Writing – original draft, Visualization, Validation, Software, Methodology, Investigation, Formal analysis, Data curation, Conceptualization. **Henrique Barros:** Writing – original draft, Validation, Software, Methodology, Formal analysis. **Miguel A. Machado:** Writing – review & editing, Validation, Methodology, Investigation, Formal analysis. **João P. Oliveira:** Writing – review & editing, Validation, Funding acquisition, Formal analysis. **Valdemar R. Duarte:** Writing – review & editing, Validation, Software, Investigation, Formal analysis, Data curation. **Telmo G. Santos:** Writing – review & editing, Visualization, Validation, Supervision, Resources, Project administration, Methodology, Funding acquisition, Formal analysis, Conceptualization.

Declaration of competing interest

The authors declare that they have no known competing financial interests or personal relationships that could have appeared to influence the work reported in this paper.

Acknowledgments

Authors acknowledge the Portuguese Fundação para a Ciência e a Tecnologia (FCT - MCTES) for its financial support via the projects: UIDB/00667/2020 and UIDP/00667/2020 (UNIDEMI). JPO acknowledges funding by national funds from FCT - Fundação para a Ciência e a

Tecnologia, I.P., in the scope of the projects: LA/P/0037/2020, UIDP/50025/2020 and UIDB/50025/2020 of the Associate Laboratory Institute of Nanostructures, Nanomodelling and Nanofabrication – i3N. This activity has received funding from the European Institute of Innovation and Technology (EIT) – Project Smart WAAM: Microstructural Engineering and Integrated Non-Destructive Testing. This body of the European Union receives support from the European Union's Horizon 2020 research and innovation programme.

Data availability

Data will be made available on request.

References

[1] S.W. Williams, F. Martina, A.C. Addison, J. Ding, G. Pardal, P. Colegrove, Wire + Arc additive manufacturing, Mater. Sci. Technol. (united Kingdom) 32 (2016) 641–647, https://doi.org/10.1179/1743284715Y.0000000073.

[2] T. DebRoy, H.L. Wei, J.S. Zuback, T. Mukherjee, J.W. Elmer, J.O. Milewski, A. M. Beese, A. Wilson-Heid, A. De, W. Zhang, Additive manufacturing of metallic components – Process, structure and properties, Prog. Mater. Sci. 92 (2018) 112–224, https://doi.org/10.1016/j.pmatsci.2017.10.001.

[3] R.R. Dehoff, M. Kirka, W.J. Sames, H. Bilheux, A.S. Tremsin, L.E. Lowe, S.S. Babu, Site specific control of crystallographic grain orientation through electron beam additive manufacturing, Mater. Sci. Technol. (united Kingdom) 31 (2015) 931–938, https://doi.org/10.1179/1743284714Y.0000000734.

[4] X. Gong, T. Anderson, K. Chou, Review on powder-based electron beam additive manufacturing Technology, Manuf. Rev. 1 (2014), https://doi.org/10.1051/mfreview/2014001.

[5] H. Gong, K. Rafi, H. Gu, T. Starr, B. Stucker, Analysis of defect generation in Ti-6Al-4V parts made using powder bed fusion additive manufacturing processes, Addit. Manuf. 1 (2014) 87–98, https://doi.org/10.1016/j.addma.2014.08.002.

[6] W. Fan, Y. Peng, Y. Qi, H. Tan, Z. Feng, Y. Wang, F. Zhang, X. Lin, Partially melted powder in laser based directed energy deposition: Formation mechanism and its influence on microstructure, Int. J. Mach. Tools Manuf. 192 (2023) 104072, https://doi.org/10.1016/j.ijmachtools.2023.104072.

[7] D. Herzog, V. Seyda, E. Wycisk, C. Emmelmann, Additive manufacturing of metals, Acta Mater. 117 (2016) 371–392, https://doi.org/10.1016/j.actamat.2016.07.019.

[8] L. Gao, A.C. Chuang, P. Kenesei, Z. Ren, L. Balderson, T. Sun, An operando synchrotron study on the effect of wire melting state on solidification microstructures of inconel 718 in wire-laser directed energy deposition, Int. J. Mach. Tools Manuf. 194 (2023) 104089, https://doi.org/10.1016/j.ijmachtools.2023.104089.

[9] M. Papaelias, I. Segovia, F. Pedro, M. García, Review on additive manufacturing and non-destructive testing, J. Manuf. Syst. 66 (2023) 260–286, https://doi.org/10.1016/j.jmsy.2022.12.005.

[10] L. Wang, Q. Guo, L. Chen, W. Yan, In-situ experimental and high-fidelity modeling tools to advance understanding of metal additive manufacturing, Int. J. Mach. Tools Manuf. 193 (2023) 104077, https://doi.org/10.1016/j.ijmachtools.2023.104077.

[11] B. Wu, Z. Pan, D. Ding, D. Cuiuri, H. Li, J. Xu, J. Norrish, A review of the wire arc additive manufacturing of metals: properties, defects and quality improvement, J. Manuf. Process. 35 (2018) 127–139, https://doi.org/10.1016/j.jmapro.2018.08.001.

[12] C. Xia, Z. Pan, J. Polden, H. Li, Y. Xu, S. Chen, A review on wire arc additive manufacturing : Monitoring , control and a framework of automated system, J. Manuf. Syst. 57 (2020) 31–45, https://doi.org/10.1016/j.jmsy.2020.08.008.

[13] D.S.M. Serrati, M.A. Machado, J.P. Oliveira, T.G. Santos, Non-Destructive Testing Inspection for Metal Components Produced Using Wire and Arc Additive Manufacturing, Metals (basel). 13 (2023), https://doi.org/10.3390/met13040648.

[14] T. Hauser, R.T. Reisch, P.P. Breese, B.S. Lutz, M. Pantano, Y. Nalam, K. Bela, T. Kamps, J. Volpp, A.F.H. Kaplan, Porosity in wire arc additive manufacturing of aluminium alloys, Addit. Manuf. 41 (2021) 101993, https://doi.org/10.1016/j.addma.2021.101993.

[15] P.A. Colegrove, F. Martina, M.J. Roy, B.A. Szost, S. Terzi, S.W. Williams, P. J. Withers, D. Jarvis, High pressure interpass rolling of Wire + Arc additively manufactured titanium components, Adv. Mater. Res. 996 (2014) 694–700, https://doi.org/10.4028/www.scientific.net/AMR.996.694.

[16] Y. Xie, H. Zhang, F. Zhou, Improvement in Geometrical Accuracy and Mechanical Property for Arc-Based Additive Manufacturing Using Metamorphic Rolling Mechanism, J. Manuf. Sci. Eng. Trans. ASME. 138 (2016) 1–8, https://doi.org/10.1115/1.4032079.

[17] V.R. Duarte, T.A. Rodrigues, N. Schell, R.M. Miranda, J.P. Oliveira, T.G. Santos, Hot forging wire and arc additive manufacturing (HF-WAAM), Addit. Manuf. 35 (2020) 101193, https://doi.org/10.1016/j.addma.2020.101193.

[18] F.W.C. Farias, V.R. Duarte, I.O. Felice, J. da C.P. Filho, N. Schell, E. Maawad, J.A. Avila, J.Y. Li, Y. Zhang, T.G. Santos, J.P. Oliveira,, In situ interlayer hot forging arc-based directed energy deposition of Inconel® 625: process development and microstructure effects, Addit. Manuf. 66 (2023), https://doi.org/10.1016/j.addma.2023.103476.

[19] F.W.C. Farias, V.R. Duarte, I.O. Felice, J. da C.P. Filho, N. Schell, E. Maawad, J.Y. Li, Y. Zhang, T.G. Santos, J.P. Oliveira,, In situ interlayer hot forging arc plasma directed energy deposition of Inconel® 625: microstructure evolution during heat treatments, J. Alloys Compd. 952 (2023), https://doi.org/10.1016/j.jallcom.2023.170059.

[20] P. Urhal, A. Weightman, C. Diver, P. Bartolo, Robot assisted additive manufacturing: A review, Robot. Comput. Integr. Manuf. 59 (2019) 335–345, https://doi.org/10.1016/j.rcim.2019.05.005.

[21] D. Ding, Z. Pan, D. Cuiuri, H. Li, S. Van Duin, N. Larkin, Bead modelling and implementation of adaptive MAT path in wire and arc additive manufacturing, Robot. Comput. Integr. Manuf. 39 (2016) 32–42, https://doi.org/10.1016/j.rcim.2015.12.004.

[22] A.U. Khan, Y.K. Madhukar, An Economic Design and Development of the Wire Arc Additive Manufacturing Setup, in, Procedia CIRP, Elsevier (2020) 182–187, https://doi.org/10.1016/j.procir.2020.02.166.

[23] F. Li, S. Chen, Z. Wu, Z. Yan, Adaptive process control of wire and arc additive manufacturing for fabricating complex-shaped components, Int. J. Adv. Manuf. Technol. 96 (2018) 871–879, https://doi.org/10.1007/s00170-018-1590-0.

[24] L. Yuan, D. Ding, Z. Pan, Z. Yu, B. Wu, S. Van Duin, H. Li, W. Li, Application of multidirectional robotic wire arc additive manufacturing process for the fabrication of complex metallic parts, IEEE Trans. Ind. Informatics. 16 (2020) 454–464, https://doi.org/10.1109/TII.2019.2935233.

[25] S. Radel, A. Diourte, F. Soulié, O. Company, C. Bordreuil, Skeleton arc additive manufacturing with closed loop control, Addit. Manuf. 26 (2019) 106–116, https://doi.org/10.1016/j.addma.2019.01.003.

[26] W.S. Lim, A.G. Dharmawan, G.S. Soh, Development and performance evaluation of a hybrid-wire arc additive manufacturing system based on robot manipulators, Mater. Today Proc. 70 (2022) 587–592, https://doi.org/10.1016/j.matpr.2022.09.608.

[27] P. Sokolov, A. Aleshchenko, A. Koshmin, V. Cheverikin, P. Petrovskiy, A. Travyanov, A. Sova, Effect of hot rolling on structure and mechanical properties of Ti-6Al-4V alloy parts produced by direct laser deposition, Int. J. Adv. Manuf. Technol. 107 (2020) 1595–1603, https://doi.org/10.1007/s00170-020-05132-0.

[28] Z.X. Zhang, S.J. Qu, A.H. Feng, J. Shen, D.L. Chen, Hot deformation behavior of Ti-6Al-4V alloy: Effect of initial microstructure, J. Alloys Compd. 718 (2017) 170–181, https://doi.org/10.1016/j.jallcom.2017.05.097.

[29] X. Fang, L. Zhang, G. Chen, K. Huang, F. Xue, L. Wang, J. Zhao, B. Lu, Microstructure evolution of wire-arc additively manufactured 2319 aluminum alloy with interlayer hammering, Mater. Sci. Eng. a. 800 (2021) 140168, https://doi.org/10.1016/j.msea.2020.140168.

[30] J. Ma, Y. Zhang, J. Li, D. Cui, Z. Wang, J. Wang, Microstructure and mechanical properties of forging-additive hybrid manufactured Ti–6Al–4V alloys, Mater. Sci. Eng. a. 811 (2021) 140984, https://doi.org/10.1016/j.msea.2021.140984.

[31] P.A. Colegrove, H.E. Coules, J. Fairman, F. Martina, T. Kashoob, H. Mamash, L. D. Cozzolino, Microstructure and residual stress improvement in wire and arc additively manufactured parts through high-pressure rolling, J. Mater. Process. Technol. 213 (2013) 1782–1791, https://doi.org/10.1016/j.jmatprotec.2013.04.012.

[32] C. Hopper, C.I. Pruncu, P.A. Hooper, Z. Tan, S. Te Yang, Y. Liu, J. Jiang, The effects of hot forging on the preform additive manufactured 316 stainless steel parts, Micron. 143 (2021), https://doi.org/10.1016/j.micron.2021.103026.

[33] L.X. Meng, H.J. Yang, S.G. Wang, H.B. Ji, X.H. Shao, Z.J. Zhang, D.C. Ren, X. Zhang, J.B. Yang, X.H. An, Y.T. Pei, J.T.M. De Hosson, R. Yang, Z.F. Zhang, Defect-healing of a laser-powder bed fusion Ti6Al4V alloy via electro-assisted micro-forging, Mater. Charact. 205 (2023), https://doi.org/10.1016/j.matchar.2023.113298.

[34] X. Xiong, X. Qin, L. Hua, G. Wan, Z. Hu, M. Ni, Microstructure evolution and parameters optimization of follow-up hammering-assisted hybrid wire arc additive manufacturing, J. Manuf. Process. 84 (2022) 681–696, https://doi.org/10.1016/j.jmapro.2022.10.031.

[35] X. Xiong, Z. Hu, X. Qin, X. Du, G. Wan, M. Ni, D. Hu, F. Ji, L. Hua, In-situ fabrication of repairing layers for large structures using follow-up hot-hammering-assisted wire arc additive manufacturing, J. Manuf. Process. 94 (2023) 387–402, https://doi.org/10.1016/j.jmapro.2023.03.023.

[36] J.R. Hönnige, P. Colegrove, S. Williams, Improvement of microstructure and mechanical properties in Wire + Arc Additively Manufactured Ti-6Al-4V with Machine Hammer Peening, Procedia Eng. 216 (2017) 8–17, https://doi.org/10.1016/j.proeng.2018.02.083.

[37] M. Saremi, H. Arabi, B. Mohammad Sadeghi, B. Mirzakhani, K. Yousefipour, Constitutive Modeling and Microstructural Investigations for Evaluating Hot Deformation Behavior of Additively Manufactured Inconel 718 Superalloy, J. Mater. Eng. Perform. (2023), https://doi.org/10.1007/s11665-023-08866-6.

[38] X. Xiong, X. Qin, F. Ji, Z. Hu, L. Hua, Microstructure and Mechanical Properties of Wire + Arc Additively Manufactured Mild Steel by Welding with Trailing Hammer Peening, Steel Res. Int. 92 (2021) 1–11, https://doi.org/10.1002/srin.202100238.

[39] S. Sahu, B.B. Choudhury, B.B. Biswal, A Vibration Analysis of a 6 Axis Industrial Robot Using FEA, Mater. Today Proc. 4 (2017) 2403–2410, https://doi.org/10.1016/j.matpr.2017.02.090.

[40] B. Claudiu, C. Mehdi, G. Alain, K. Jean-Yves, Dynamic behavior analysis for a six axis industrial machining robot, Adv. Mater. Res. 423 (2012) 65–76, https://doi.org/10.4028/www.scientific.net/AMR.423.65.

[41] O. Ayari, A. Bouali, P.J. Méausoone, Cutting forces and accuracy characterization during wood machining with serial robots, Eur. J. Wood Wood Prod. 78 (2020) 767–775, https://doi.org/10.1007/s00107-020-01539-4.

[42] I.F. Onstein, O. Semeniuta, M. Bjerkeng, D.U. Robot, Manipulators: A Review, in,, 3rd Int, Symp. Small-Scale Intell. Manuf. Syst. SIMS 2020 (2020) 2020, https://doi.org/10.1109/SIMS49386.2020.9121490.

[43] M.E. Matour, C. Thormann, A. Winkler, Force Controlled Deburring using a Collaborative Robot, 2022 26th Int. Conf. Methods Model. Autom. Robot. MMAR 2022 - Proc. (2022) 425–429. DOI: 10.1109/MMAR55195.2022.9874311.

[44] N. Mendes, P. Neto, A. Loureiro, A.P. Moreira, Machines and control systems for friction stir welding: A review, Mater. Des. 90 (2016) 256–265, https://doi.org/10.1016/j.matdes.2015.10.124.

[45] K. Kolegain, F. Leonard, S. Zimmer-Chevret, A. Ben Attar, G. Abba, A feedforward deflection compensation scheme coupled with an offline path planning for robotic friction stir welding, IFAC-PapersOnLine. 51 (2018) 728–733, https://doi.org/10.1016/j.ifacol.2018.08.405.

[46] S. Ivanov, T. Zudilova, L. Ivanova, Z. Meleshkova, T. Voitiuk, Vibration Protection of the Robotic Arm from External Effects on the Base, in, Conf. Open Innov. Assoc. Fruct (2020) 514–522. https://fruct.org/publications/acm26/files/Iva2.pdf.

[47] C. Dumas, S. Caro, S. Garnier, B. Furet, Joint stiffness identification of six-revolute industrial serial robots, Robot. Comput. Integr. Manuf. 27 (2011) 881–888, https://doi.org/10.1016/j.rcim.2011.02.003.

[48] J. Qin, F. Léonard, G. Abba, Real-Time Trajectory Compensation in Robotic Friction Stir Welding Using State Estimators, IEEE Trans. Control Syst. Technol. 24 (2016) 2207–2214, https://doi.org/10.1109/TCST.2016.2536482.

[49] M. Leonesio, E. Villagrossi, M. Beschi, A. Marini, G. Bianchi, N. Pedrocchi, L. M. Tosatti, V. Grechishnikov, Y. Ilyukhin, A. Isaev, Vibration Analysis of Robotic Milling Tasks, Procedia CIRP. 67 (2018) 262–267, https://doi.org/10.1016/j.procir.2017.12.210.

[50] V. Nguyen, J. Johnson, S. Melkote, Active vibration suppression in robotic milling using optimal control, Int. J. Mach. Tools Manuf. 152 (2020) 103541, https://doi.org/10.1016/j.ijmachtools.2020.103541.

[51] J. Hu, A.M. Kabir, S.M. Hartford, S.K. Gupta, P.R. Pagilla, Robotic deburring and chamfering of complex geometries in high-mix/low-volume production applications, IEEE Int. Conf. Autom. Sci. Eng. (2020-Augus (2020)) 1155–1160, https://doi.org/10.1109/CASE48305.2020.9217042.

[52] J. Zhao, Y. Duan, B. Xie, Z. Zhang, FSW robot system dimensional optimization and trajectory planning based on soft stiffness indices, J. Manuf. Process. 63 (2021) 88–97, https://doi.org/10.1016/j.jmapro.2020.05.004.

[53] N. Mendes, P. Neto, M.A. Simão, A. Loureiro, J.N. Pires, A novel friction stir welding robotic platform: welding polymeric materials, Int. J. Adv. Manuf. Technol. 85 (2014) 37–46, https://doi.org/10.1007/s00170-014-6024-z.

[54] V.R. Duarte, T.A. Rodrigues, N. Schell, R.M. Miranda, J.P. Oliveira, T.G. Santos, In-situ hot forging directed energy deposition-arc of CuAl8 alloy, Addit. Manuf. 55 (2022) 102847, https://doi.org/10.1016/j.addma.2022.102847.

[55] T.A. Rodrigues, J.D. Escobar, J. Shen, V.R. Duarte, G.G. Ribamar, J.A. Avila, E. Maawad, N. Schell, T.G. Santos, J.P. Oliveira, Effect of heat treatments on 316 stainless steel parts fabricated by wire and arc additive manufacturing: Microstructure and synchrotron X-ray diffraction analysis, Addit. Manuf. 48 (2021) 102428, https://doi.org/10.1016/j.addma.2021.102428.

[56] P.P. Fonseca, V.R. Duarte, F.W.C. Farias, B.S. Cota, T. Silva, T.G. Santos, C. M. Machado, Enhancing manufacturing and post-processing properties of WAAM ER110 HSLA steel: in situ hot forging + post-deposited heat treatment effects on surface quality and specific cutting energy, Prog. Addit. Manuf. (2024), https://doi.org/10.1007/s40964-024-00814-7.